# Non-Oxide Ceramic Additive Manufacturing Processes for Aerospace Applications

Giancarlo D'Orazio\*, Grace Falanga<sup>†</sup>, Zachariah Chazen<sup>‡</sup> *Cornell University, Ithaca, NY, 14853* 

Jason Jones§

Moog, Inc., East Aurora, NY, 14052

Sadaf Sobhani<sup>¶</sup>
Cornell University, Ithaca, NY, 14853

As the frequency of SmallSat launches continues to increase, technology solutions to enable fast, accurate, and scalable manufacturing of parts are necessary to meet the demand. In this work, additively manufactured technical ceramics are examined to meet the needs of spacecraft propulsion systems, specifically thrust chambers for use with monopropellants. This research focuses on Digital Light Processing (DLP), a lithography-based AM technique for ceramics that involves exposing a photosensitive liquid polymer resin containing a suspension of ceramic particles to UV light layer-by-layer. This work investigates non-oxide ceramics which have exceptional thermal shock resistance and mechanical strength which can improve the operational lifespan of printed thrust chambers. Commercially available oxide ceramic slurries were first trialed, serving as a baseline for comparison to in-development non-oxide ceramic slurries. Mechanical and thermal testing was performed on printed test articles to determine suitability for aerospace applications.

# I. Nomenclature

 $\begin{array}{lll} b & = & \text{beam width} \\ C & = & \text{constant} \\ D_{cure} & = & \text{depth of cure} \\ d_{beam} & = & \text{beam depth} \\ d_{part} & = & \text{particle diameter} \\ E_{dose} & = & \text{dose energy density} \\ I & = & \text{light intensity} \\ \end{array}$ 

 $I_0$  = light intensity to cure resin  $n_0$  = resin refractive index

 $\Delta_n$  = difference between refractive index of  $n_0$  and ceramic

 $P_{LED}$  = LED power

 $\phi$  = volumetric particle loading

#### **II.** Introduction

As the commercial aerospace industry continues to grow, there is a significant push to lower the cost of launch. This can be accomplished by reducing mass, thus driving an exponential increase in SmallSat launches[1]. This is largely made possible by advancements in all aspects of satellite design, but especially with materials. When designing

<sup>\*</sup>PhD Student, Sibley School of Mechanical and Aerospace Engineering

<sup>†</sup>Master of Engineering, Sibley School of Mechanical and Aerospace Engineering

<sup>\*</sup>Master of Engineering Student, Sibley School of Mechanical and Aerospace Engineering

<sup>§</sup>Advanced Programs Engineer

<sup>¶</sup>Assistant Professor, Mechanical and Aerospace Engineering, AIAA Member.

an in-space propulsion system for thrust chambers are required to maintain their structural integrity in the harsh environments of space, the rapid heating when the thrusters are fired, and presence of highly corrosive monopropellants such as hydrazine and new green propellants, namely hydroxyl ammonium nitrate (HAN). Thus, thrusters that exhibit excellent thermal properties, corrosion resistance and strength are desired. High-performance ceramic materials are utilized in a variety of technical applications that necessitate such properties such as porous media burners[2], thermal protection systems[3], and transpiration cooling systems for hypersonic conditions[4]. While ceramics may seem to be the optimal material for SmallSat thrust chambers, there are still challenges associated with replacing the currently used platinum group metals or refractory alloys. For instance, ceramics are typically quite brittle, making them more difficult to use in high-force applications like high-pressure thrust chambers[5]. Additionally, the startup costs associated with conventional manufacturing techniques are typically very high[6], thus a high yield is required in order to make the manufacturing process cost-effective. While the number of SmallSat launches is on a steady increase, it is still a much lower volume than what is typical for conventional ceramic techniques. Along with this, there is high variability in the requirements and designs of SmallSat components for each satellite which is incongruous with traditional casting techniques for manufacturing. As a result, additive manufacturing (AM) is regarded as a promising manufacturing technique to allow for low-cost low-volume production while increasing design flexibility[7].

Photopolymerization-based AM technologies such as Lithography-based Ceramic Manufacturing (LCM) and Digital Light Processing (DLP) are well-suited to the manufacture of small complex ceramic parts with high resolution and excellent surface finish[7]. In these manufacturing methods, a photosensitive slurry is made containing ceramic powders, photoinitiator, monomer, and dispersant. The slurry is then exposed to UV light layer-by-layer to create a green part in the shape of the final design. From there, the polymer matrix is burned out and the ceramic powder is then sintered to create a dense ceramic part[8]. These technologies are good options for SmallSat thruster applications due in part to their high industrial readiness level and speed of manufacture[7]. Additionally, they are capable of producing high-quality finished parts with over 99% density[7] and comparable strength to conventionally manufactured parts[9].

Alumina ( $Al_2O_3$ ) is one of the most common choices of ceramic material for light-based AM of ceramics for a number of reasons. First, its refractive index at 405 nm is approximately 1.79 which matches with most methacrylate resins which range between 1.4 and 1.7 [10, 11]. Further, compared to high-strength technical ceramics, alumina has a lower sintering temperature without special atmosphere requirements - typically 1500-1700°C in ambient air for alumina compared to over 1700°C in a pressurized nitrogen atmosphere for silicon nitride ( $Si_3N_4$ ) [7, 12, 13]. While alumina is able to withstand operating temperatures of up to 1900°C[2], its poor thermal shock resistance ( 200°C[14]) makes it less desirable choice for an in-space thruster as it would likely crack. By adding  $SiO_2$  to alumina, the thermal shock resistance can be improved[2], however non-oxide ceramics such as  $Si_3N_4$  are able to withstand much higher temperatures and thermal shocks ( $\Delta T>800$ °C[15]) in addition to higher hardness and strength, which make them superior for these applications[16]. However, non-oxide ceramics like  $Si_3N_4$  have much higher sintering temperatures and require atmospheres other than air[7]. Poor optical properties including high absorption and a high refractive index, making light-based printing methods much more difficult[17]. In general, the depth of cure for photosensitive resins with solid loading can be approximated in Equation 1:

$$D_{cure} \approx \frac{C}{\phi} \cdot d_{part} \left(\frac{n_0}{\Delta_n}\right)^2 \cdot ln\left(\frac{I}{I_0}\right) \tag{1}$$

Where  $D_{cure}$  is the depth of cure, C is a constant, typically wavelength,  $\phi$  is the volumetric particle load,  $d_{part}$  is the particle diameter,  $n_0$  is the refractive index of the base resin,  $\Delta_n$  is the difference between the refractive index of  $n_0$  and the ceramic particles, I is light intensity, and  $I_0$  is the light intensity required to cure the resin. Thus larger mismatches between the refractive index of the resin and ceramic will require considerably higher light intensity to produce the same cure thickness. Table 1 shows the refractive indices of the development resin used in slurry creation as well as some selected ceramics.

Table 1 Refractive indices of selected materials in 405 nm wavelength light

Material	Refractive Index	Source	
Development Resin C	1.46	Admatec	
Silica (SiO <sub>2</sub> )	1.470	Malitson et al., 1965 [18]	
Alumina (Al <sub>2</sub> O <sub>3</sub> )	1.786	Malitson et al., 1958 [19]	
Silicon nitride (Si <sub>3</sub> N <sub>4</sub> )	2.098	Luke et al. [20]	
Aluminum nitride (AlN)	2.249	Pastrňák et al. [21]	
Silicon carbide (SiC)	3.519	Larruquert et al. [22]	

Recent work in DLP printing has focused on developing ways to successfully print non-oxide ceramics, and a number of studies have been successful. Montanari demonstrated the ability to produce Si<sub>3</sub>N<sub>4</sub> ceramic components via lithography-based AM[23]. Huang et al. produced Si<sub>3</sub>N<sub>4</sub> parts via DLP and achieved >90% dense final parts[24] and Altun et al. improved on this density by printing SiAlON parts instead[9]. Most recently, work by Yang et al. demonstrated a process for printing Si<sub>3</sub>N<sub>4</sub> that has been surface modified via oxidation to produce SiO<sub>2</sub> which decreases light absorptivity [25]. Work has also been done to print in aluminum nitride (AlN) with one study focusing on modifying the surface of the AlN powders in suspension to improve the stability and rheological properties of the suspension[26]. Ożóg et al. successfully manufactured parts made of AlN, but found difficulty with geometrical accuracy[27]. Due to greater difficulties in processing AlN, this investigation will focus on Si<sub>3</sub>N<sub>4</sub> as opposed to AlN. Further, the focus of this work is to develop a functional slurry without modifications to precursor powders, ensuring sintered products are of a well established quality and structure.

This work aims to develop a reliable method for manufacturing fully dense ceramic components using digital light processing (DLP) for SmallSat thruster applications. The thermal shock characteristics of commercially available oxide ceramic slurries were tested and sample thrusters were printed for comparison to conventionally manufactured parts. Further, a method for developing  $Si_3N_4$  slurry is developed as well as proposed debinding and sintering curves. Importantly, this work aims to show that pure  $\beta$ -phase  $Si_3N_4$  can be produced from an AM process, resulting in high strength parts which are fracture resistant.

#### III. Material Design and Manufacturing

The Admatec Admaflex 130 DLP print was selected to conduct trials with alumina, mullite, and  $Si_3N_4$ . These ceramic slurries are composed of a combination of photosensitive resin and ceramic particles with approximately 40% ceramic loading by mass. The printer utilizes a high resolution projector system to photopolymerize the slurry with 405 nm wavelength light. The system is capable of layer heights as small as 10 µm with a minimum feature size of 50 µm while offering a print volume of 96 x 54 x 100 mm. In normal operation, slurry is held in a vat atop a 40 µm thick plastic foil. This foil transports a layer of slurry four times the thickness of the desired layer height across the projector where the build head subsequently moves down and the image is projected through the slurry to the build plate. The printer setup is shown in Figure 1. Additionally, a static vat style system, which does not use the rolling foil system, was fabricated for use with the printer. This vat reduces the minimum volume of slurry required for small batch printing, and is therefore well suited to small-batch slurry development. For alumina and mullite testing the standard foil system was used, whereas the  $Si_3N_4$  parts were printed with the vat system.

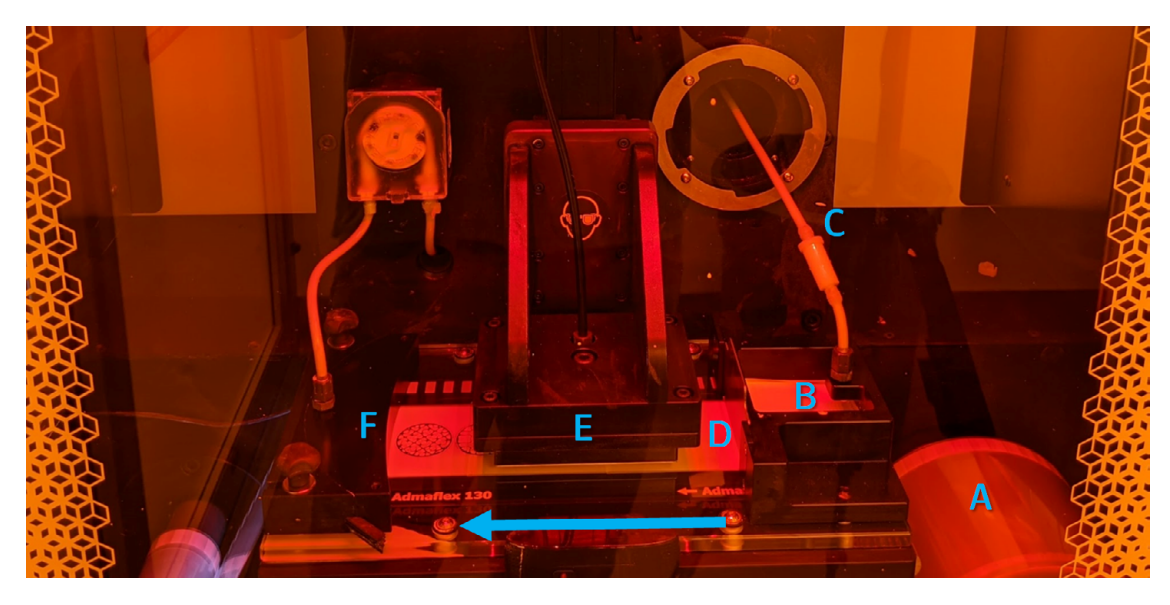


Fig. 1 The Admaflex 130 printer pulls a foil roll (A) underneath a vat of slurry (B) which is replenished through a recirculation system and filter (C). When the foil moves through the printer, a gate allows a layer four times thicker than the layer height to deposit on the foil (D) which is then moved below the print head (E) where parts are exposed. After exposure, residual slurry is collected (F) and pumped back to the slurry vat (B). The foil moves in the direction of the arrow.

After printing, the parts are rinsed in 99% propanol to remove any excess uncured slurry and then placed in a deionized water soak for 24 hours at  $40^{\circ}$ C. This step, called water debinding, removes some of the water-soluble resin used in the printing process, reducing some of the resin load before thermal debinding. After this, the parts are placed on damp towels to allow the parts to dry slowly and evenly. Once dry, parts undergo thermal debinding to remove any remaining resin before the sintering process. After these steps, processing for the oxide and non-oxide ceramics differ substantially, with lower temperature air atmosphere used for the oxide ceramics, while the  $Si_3N_4$  requires differing debinding and sintering curves and an nitrogen atmosphere.

#### A. Oxide Ceramics

Two commercially available slurries were used for fabrication of the oxide ceramics: Admaprint A130 ( $Al_2O_3$ ) and Slurry  $Al_2O_3$  95 (referred to as mullite, 95%  $Al_2O_3$  and 5%  $SiO_2$ ). Prototype thrust chambers were printed first in alumina and then in mullite. Prior to each print, a depth of cure confirmation test was carried out, where a sample of slurry was exposed to light at the power and length of time to be used during the print. The excess slurry was wiped off and the cured layer was measured with a digital micrometer to ensure a cure depth of at least  $60\mu m$ , double the desired layer height ( $30\mu m$ ).

Thrust chambers made of alumina and mullite were thermally shocked based on the ASTM C1525-18 water quenching procedure to achieve a  $\Delta T$  of 400°C and then 700°C[15]. Two different geometries were trialed, as shown in Figure 2. After thermal shock, the thrust chambers were dried off and died with fountain pen ink to better reveal any cracking.

Test beams were subsequently printed out of each material in order to characterize the flexural strength of the two oxide ceramics and impact of thermal shock. Beams were designed according to ASTM C1161-18 standard configuration B, with a total beam length of 45 mm, width of 4 mm and depth of 3 mm [28]. A subset were thermally shocked based via water quenching to a  $\Delta T$  of 400°C and 700°C based on ASTM C1525-18 [15]. Test bars were printed in two different orientations, with the Z-orientation referring to samples printed with layer lines perpendicular to the bending orientation and the XY-orientation referring to samples printed with layer lines parallel to the bending orientation. Flexural strength testing was performed using an Instron 5969 with a 5kN load cell in a four-point bend test configuration as described in ASTM C1161-18 [28]. Each of these tests was performed a minimum of 3 times to get an average beam strength.

#### **B. Silicon Nitride**

Admaprint Blank Resin C (Admatec) was used for the development of  $Si_3N_4$  parts.  $Si_3N_4$  powder, SN-E05 grade  $\alpha$ - $Si_3N_4$  (Ube) was mixed with sintering aids  $Al_2O_3$  (MSE Supplies, 99.99% purity, 500 nm) and  $Y_2O_3$  (US Research Nanomaterials, Inc., 99.99% purity, 30-45 nm). These powders were combined in a 92:5:3 mass ratio. This formulation enables liquid-state sintering, which lowers sintering temperatures while maintaining high strength.  $Al_2O_3$  and  $Y_2O_3$  are added to  $\alpha$ - $Si_3N_4$  which, when sintered, form liquid silicates. These liquid silicates subsequently precipitate solid  $\beta$ - $Si_3N_4$ , the stronger of the two forms. Furthermore, utilizing  $\alpha$ - $Si_3N_4$  and applying the correct sintering profile will yield finished parts with high fracture toughness due to the long hexagonal crystals formed by this process [29, 30].

To ensure the ceramic particles remained suspended in the slurry, 2 wt % of Hypermer KD1 powder dispersant was dissolved in 20 wt% of acetone and added to the ceramic powders, fully incorporating the solvent by mixing with a glass stir rod and adding extra acetone until the mixture was fully wet. A  $Si_3N_4$  milling ball was added to the bottle and the mixture was then milled for 1 hour in a Spex 8000 Mixer/Mill ball mill, in 30 minute increments with 5 minute rest between. After ball milling, the mixture was dried, milled, and sifted, and the blank resin was added to make a mixture of 40% solids by mass. A milling ball was added to aid in mixing the slurry, and it was placed on a roller to fully incorporate for at least 1 hour prior to use.

In order to ensure the prepared slurry exhibits shear thinning behavior and has an acceptable viscosity to print on the Admaflex 130, the viscosity was measured using a frequency sweep on a TA Instruments DHR3 Rheometer. With a 40 mm parallel plate attachment and a 1 mm gap for testing. The shear rate was varied from  $10^{-3}$  to  $10^2$  s<sup>-1</sup>, with eight points collected per decade. All experiments were performed at room temperature.

Based on Equation 1, The developed  $Si_3N_4$  slurries required robust depth of cure testing in order to determine the lowest exposure time and LED power that would result in the minimum cure depth of 60  $\mu$ m. This cure depth is twice that of the designed layer thickness for most prints, ensure proper interlayer adhesion. In this test, samples of slurry were exposed over a range of exposure times and LED powers, as described in Table 2. After each sample was exposed, the excess slurry was wiped off and the thickness was measured using a digital micrometer.

To ensure all binding particles and other contaminates are removed before sintering an AM ceramic, thermogravimetric analysis (TGA) was conducted. The temperature of the ceramic part was raised at a rate of 1°C/Minute until it reached 1000°C, measuring weight every three seconds. This experiment was performed twice, once in air and again in a nitrogen environment. This was done so that the mass percent over temperature could be found and more importantly the derivative weight loss could be determined. This produces peaks at which weight loss rate is highest in order to develop an optimal thermal debinding curve.

Scanning electron microscopy (SEM) and energy dispersive X-ray spectroscopy (EDS) were used to determine the microstructure of the sintered ceramics as well as general material composition. In general, ceramic samples were imaged first without a coating to determine if charging would be problematic, as imaging without coating can yield better EDS results. Both a Zeiss Supra SEM and Zeiss LEO 1550 were used for SEM imaging; the microscopes were paired with Bruker EDS modules.

X-ray diffraction (XRD) was conducted with a Bruker D8 General Area Detector Diffraction System to determine crystal phase and confirm  $Si_3N_4$  conversion from  $\alpha$ -phase to  $\beta$ -phase. Two sets of apertures were used, first a 0.5 mm aperture and later a 0.3 mm aperture to ensure fine detail collection. In the 0.5 mm aperture configuration, the sample was scanned from  $\theta = 15^{\circ}$ to 80° at 5° increments with a 60 s exposure per increment. In the 0.3 mm configuration, the exposure per increment was increased to 85 s to enhance contrast. Analysis was conducted with the Bruker DIFFRAC.EVA and MDI JADE software for data conversion and phase analysis respectively.

## IV. Results and Discussion

Figure 2 shows each nozzle dyed with ink after thermal shock testing, with cracks from the testing highlighted. At a  $\Delta T$  of 700°C, however, both parts are significantly degraded.

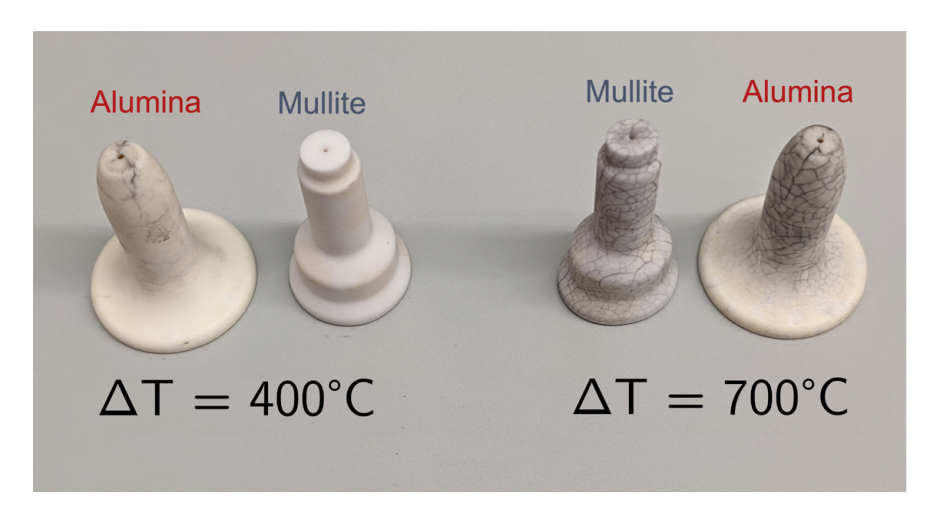


Fig. 2 Thermally shocked alumina and mullite thrust chambers dyed with ink to reveal visible cracking.

Bending stress was determined via Equation 2, where S is the flexural strength, P is the force at break, L is the outer span of the test configuration, 40 mm in this case, b is the specimen width and  $d_{beam}$  is the specimen height. The results of the bending test are shown in Figure 3 for the alumina and mullite specimens.

$$S = \frac{3PL}{4bd_{beam}^2} \tag{2}$$

For the test bars printed in the Z-orientation, none of the mullite bars survived sintering. In the alumina samples, unsurprisingly, this orientation produced samples with much lower strength than those printed in the XY-orientation. In all of the alumina samples, the thermally shocked bars had a lower strength, which agreed with expectations. Additionally, the alumina had a higher strength than the mullite before thermal shock which agrees with prior work. In the  $400^{\circ}$ C thermal shock test, the alumina outperforms mullite due to its initial higher flexural strength. However in the  $700^{\circ}$ C  $\Delta$ T test, mullite had a higher strength than the alumina.

Ultimately, while there are benefits to utilizing a material such as mullite over alumina, its thermal shock characteristics cannot match that of higher performance technical ceramics such as  $Si_3N_4$ . The higher flexural strength and thermal shock resistance of  $Si_3N_4$ , approximately three times the oxide ceramics tested, is of considerably higher importance than increased printing time. As such, the focus of this work from this point is centered on developing a repeatable AM process for printing  $Si_3N_4$  parts.

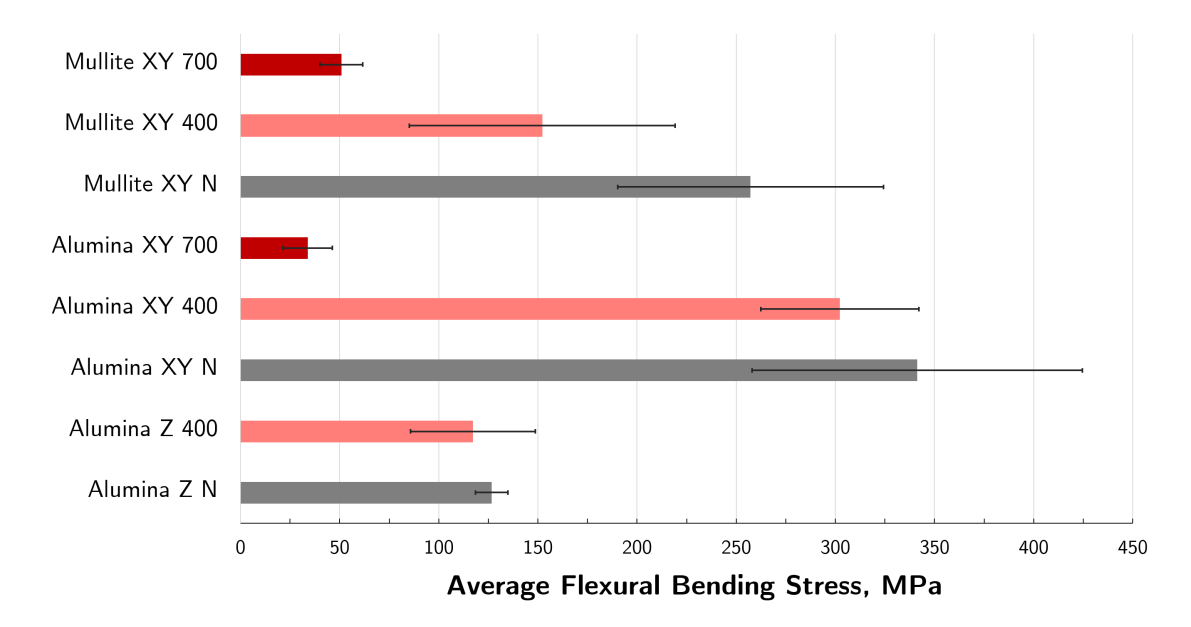


Fig. 3 Results of four point flexural bend testing on alumina and mullite test bars. Print orientations of the samples are described by XY and Z, describing samples printed with layers parallel and perpendicular to the bending orientation, respectively. Thermal shock on each sample is represented in the sample name with N indicating no shock, 400 indicating a shock with  $\Delta T$  of 400°C and 700 indicating a  $\Delta T$  of 700°C.

### A. Si<sub>3</sub>N<sub>4</sub> Testing

#### 1. Depth of Cure

Total dose energy is dependent on the length of time of dose and the set LED power of the projector. LED power is controlled on a 0-100% scale which can be roughly approximated as the dose energy density by the following equation derived from machine commissioning test:

$$E_{dose} = 0.46 * P_{LED} \tag{3}$$

Where  $E_{dose}$  is the dose energy density in mW/cm<sup>2</sup> and  $P_{LED}$  is the LED power percentage. Depth of cure tests included 3 trials per test condition to ensure the data were representative.

Table 2 Depth of cure test on Si<sub>3</sub>N<sub>4</sub> slurry, with 3 data points per test condition. Cure depths are listed in micrometers.

		Exposure Time (s)		
		5s	10s	15s
	50%	$37.33 \pm 1.2$	$53.00 \pm 4.6$	54.67 ± 3.1
LED	60%	39.67 ± 3.5	52.67 ± 2.5	59.67 ± 5.0
Power	<b>70</b> %	47.00 ± 1.0	55.33 ± 1.5	$61.33 \pm 3.5$

The results of the depth of cure test indicate that it is possible to print  $Si_3N_4$  parts with the developed slurry in a reasonable time period, requiring a minimum of  $423 \text{ mJ/cm}^2$  to attain  $60 \text{ }\mu\text{m}$  depth of cure. The impact of the poor optical properties of  $Si_3N_4$  is evident, as alumina and mullite prints are typically run at 30% LED power between 2 and 4 seconds; this results in an energy density of  $55.2 \text{ mJ/cm}^2$  at the higher end. Based on Equation 1, it is expected that  $Si_3N_4$  would require approximately 6 times the effective dose than the alumina slurry. The depth of cure tests illustrated an approximately 7.7 times increase in required effective dose. Importantly, it is possible to obtain a reasonable exposure time to achieve a cure depth of  $60 \text{ }\mu\text{m}$ , which would allow for a  $30 \text{ }\mu\text{m}$  layer height. Based on the results in Table 2, an LED power of 60 or 70% will be chosen with an exposure time of 15 seconds. This combination meets the cure depth requirements while exposing the slurry to the lowest possible power.

## 2. Rheology

Four trials of rheometer testing yielded consistent results, and shear thinning behavior was exhibited by the  $Si_3N_4$  slurry as seen along with the singular trial of the Admatec mullite slurry in Figure 4. Based on the results of the trials, the standard deviation is very small resulting in this study being easily repeatable. Additionally, the mullite and  $Si_3N_4$  slurry follow very similar slopes as shear rate is varied, with the  $Si_3N_4$  having a somewhat lower viscosity. Based on the close match between viscosity and shear thinning behavior, the  $Si_3N_4$  slurry is compatible with the Admaflex 130 printing system, allowing for consistent slurry dosing and reliable slurry recirculation.

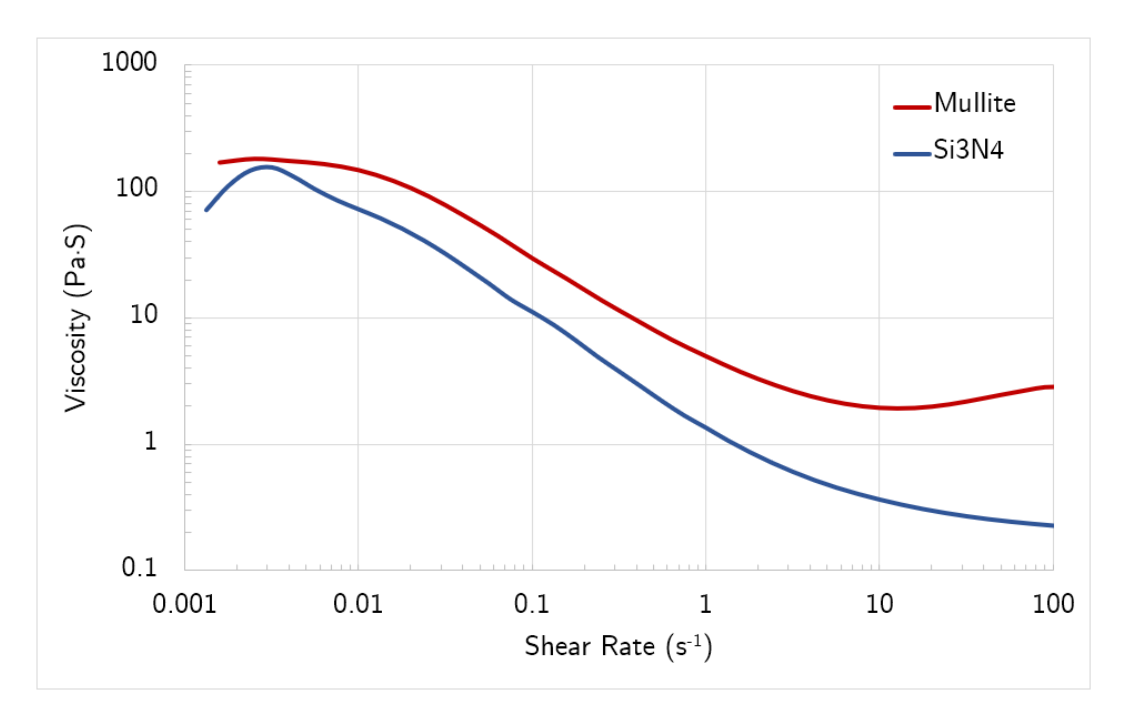


Fig. 4 Frequency sweep rheometer results for  $Si_3N_4$  slurry manufactured in house and mullite slurry from the printer manufacturer.

Distinct layer line defects were observed in the finished flexural bending beams, as shown in Figure 5. These defects appear to be a result of the static vat curing system used for small test batches. Small test prints with the foil system appeared not to contain the same defects.

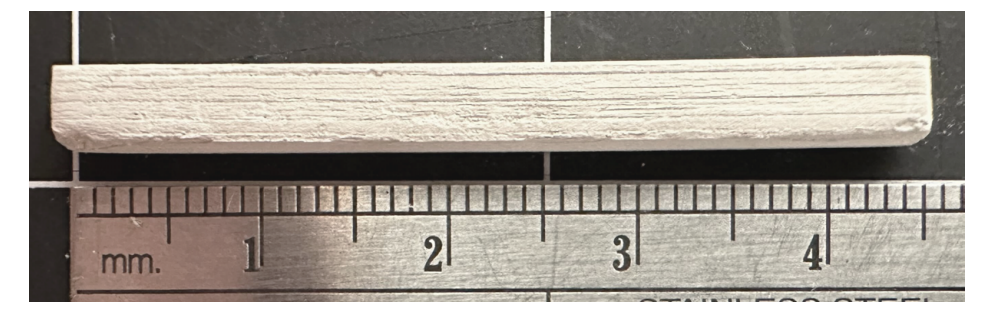


Fig. 5 Green Si<sub>3</sub>N<sub>4</sub> beam after water debinding and drying.

### 3. Thermogravimetric Analysis

Flexural bending beams were printed in Si3N4, and subsequently TGA tests were performed on the parts in air and nitrogen, the results of which can be seen in Figure 6. Based on the results of the TGA, it appears that a higher mass percent of binder is removed in the air atmosphere at the expense of a longer debinding curve with multiple holds

located at the four main peaks visible in the derivative weight loss curve. The peaks occur at approximately 190°C, 320°C, 385°C, and 435°C. By comparison, the nitrogen derivative weight loss curve peaks only at 385°C, representing a somewhat simpler debinding curve with less overall mass loss.

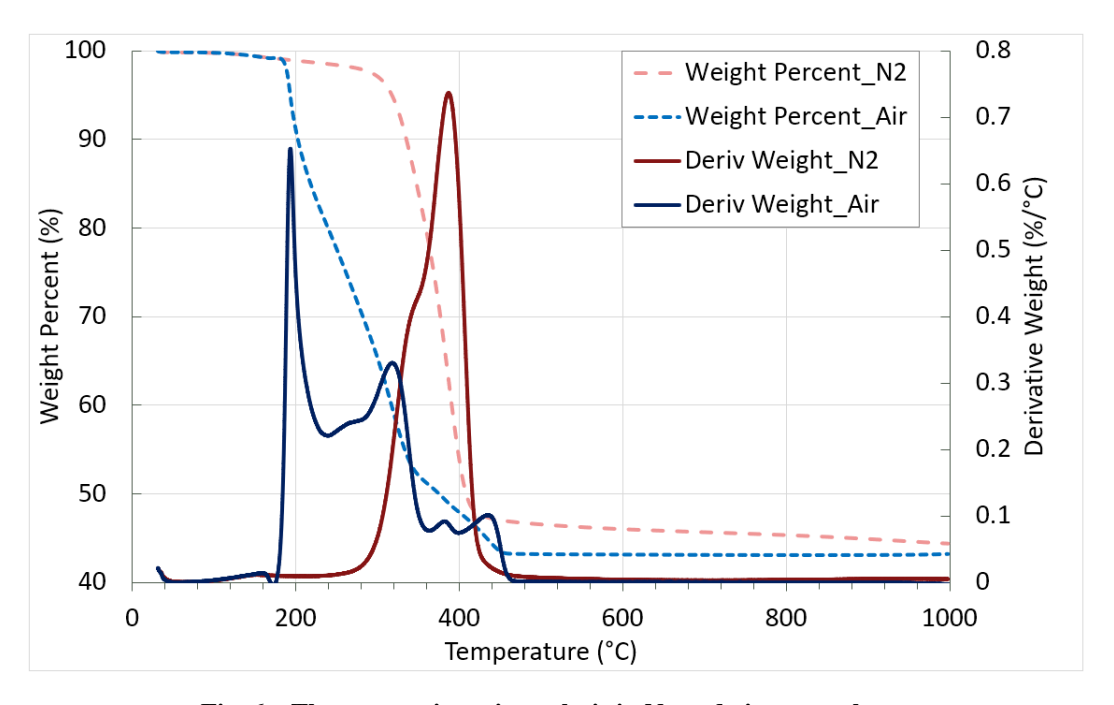


Fig. 6 Thermogravimetric analysis in N<sub>2</sub> and air atmospheres

### 4. Sintering

As demonstrated in Figure 7, the beams warped considerably following thermal processing. This appears to be due to issues with the printing process, as highlighted in Figure 5, as the distinct layer line defects contributed to low green part density and highly anisotropic parts. Final part density was determined to be approximately 70%, far below the 99% typical for oxide ceramic parts manufactured on this printer. Based on the highly deformed nature of the sintered beams, no flexural bending tests were conducted on  $Si_3N_4$  beams.



Fig. 7 Sintered beam with visible layer lines and warping due to poor interlayer adhesion

# 5. SEM and EDS

In Figure 8, the hexagonal bar-like microstructure which is characteristic of  $\beta$ -Si<sub>3</sub>N<sub>4</sub>, is apparent in the AFRL sintered samples.

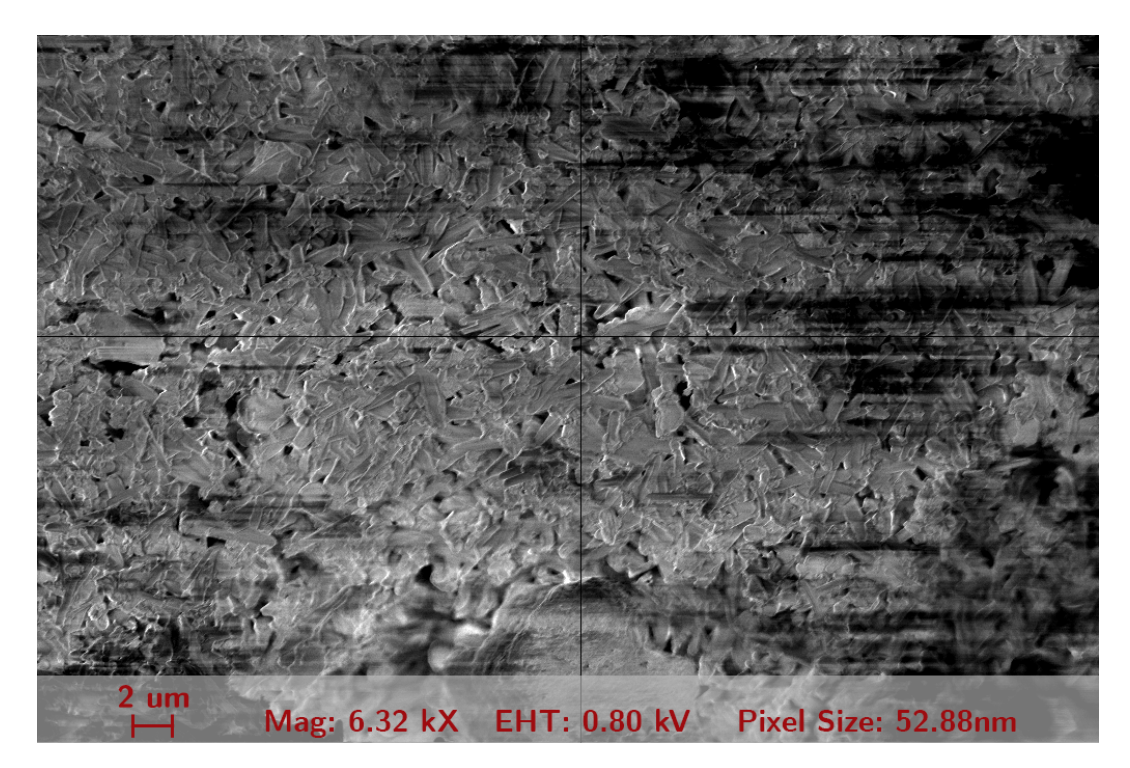


Fig. 8 SEM imagery showing the bar-like structures are characteristic of  $\beta$ -Si<sub>3</sub>N<sub>4</sub>.

EDS was conducted to determine part purity and confirm even dispersion of alumina and yttria throughout the  $Si_3N_4$ . The results in Figure 9 demonstrate well dispersed sintering aids within the  $Si_3N_4$  matrix.

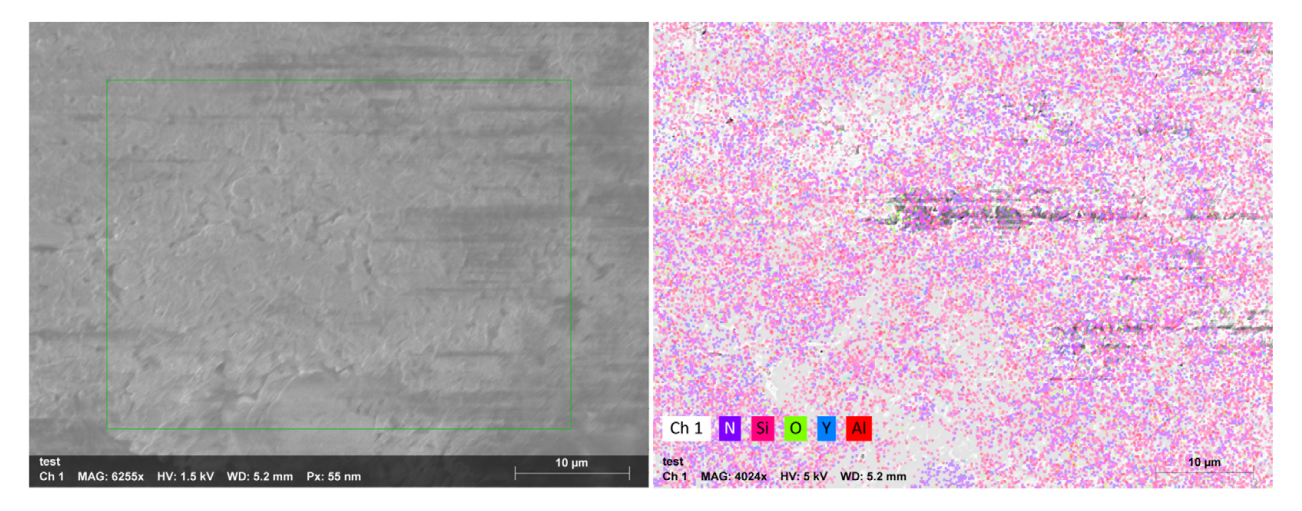


Fig. 9 SEM of the  $Si_3N_4$  bar (left) and EDS of the same region (right).

### 6. X-ray Diffraction

Figure 10 shows the XRD results from a sintered  $Si_3N_4$  test bar .MDI JADE analysis compares the derived diffraction patterns of the sample to reference patterns. In this case, the peaks shown in Figure 10 are consistent with  $\beta$ -phase  $Si_3N_4$  without any  $\alpha$ -phase peaks present. The reference peak at  $2\theta = 13.5^{\circ}$ does not correspond with the collected data as this was not included in the initial scan range of  $15^{\circ}$ to  $80^{\circ}$ . There is otherwise a high degree of agreement between the reference and derived diffraction patterns.

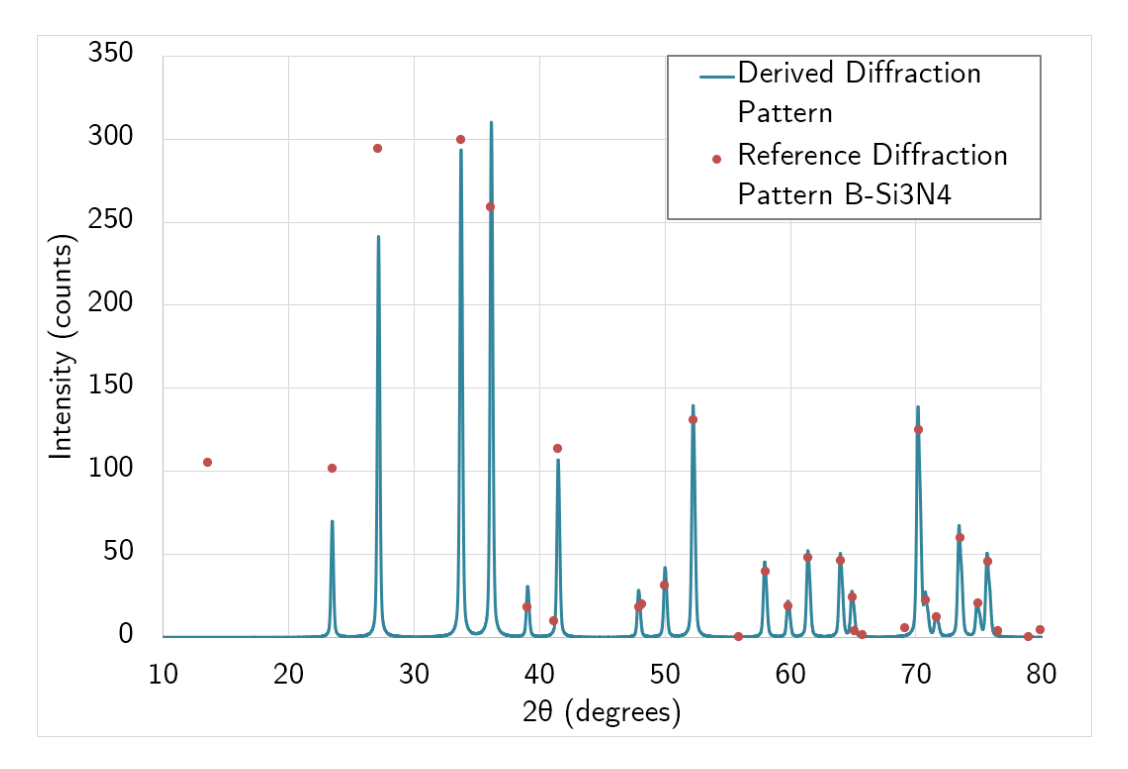


Fig. 10 X-ray diffraction results with 0.5 mm aperture. The derived diffraction pattern is based on the raw XRD data with reference points for pure  $\beta$ -Si<sub>3</sub>N<sub>4</sub>

## V. Conclusion

Initial work examined commercially available oxide ceramics and their potential for use in additively manufactured thrust chambers.  $Al_2O_3$  and mullite  $(Al_2O_3 + SiO_2)$  were tested for flexural strength and thermal shock resistance. In this case of  $Al_2O_3$ , thermal shock at 400° and 700°C resulted in an 11% and 90% decrease in flexural strength respectively. By comparison, the mullite underwent a 41% and 80% loss in strength. While the mullite represents an improvement over traditional alumina, the significant decrease in strength after shock indicates more robust materials are necessary.

This work aimed to demonstrate the feasibility of producing conventional  $Si_3N_4$  parts in a light-based AM system in spite of its higher refractive index. Adequate cure is achievable at the cost of exposure time to accommodate losses from scattering and absorption. Importantly, the minimum dose for curing at a depth of twice the print layer height is achievable without modification to a number of existing commercial printers. As such, well-established  $Si_3N_4$  formulations were found to be a good match for existing DLP systems.

Solid parts printed with  $\alpha$ -phase  $Si_3N_4$  powder were completely converted to  $\beta$ -phase, yielding stronger microstructure. It is likely that the static slurry vat used for small batch printing introduced additional stresses in the green part during printing, resulting in non-conformal layers and ultimately low final part density. It is expected that using the system with the lower stress foil system will produce uniform parts with improved interlayer adhesion, resolving the warping effect found in the sintered  $Si_3N_4$  beams. This is the focus of future work, along with further characterization of additively manufactured  $Si_3N_4$  with thermal shock, flexural bending and high pressure testing for application to space systems.

## Acknowledgments

The authors would like to acknowledge Moog, Inc. for collaboration and support. The authors would also like to acknowledge Lisa Rueschhoff, Benjamin Lam, and Connor Wyckoff of the Air Force Research Lab for their support with the development of debinding and sintering programs. This work made use of the Cornell NanoScale Facility which is supported through the NSF NNCI program (NNCI-2025233). This work also made use of the Cornell Center for Materials Research Shared Facilities which are supported through the NSF MRSEC program (DMR-1719875).

### References

- [1] Lappas, V., and Kostopoulos, V., "A Survey on Small Satellite Technologies and Space Missions for Geodetic Applications," *Satellites Missions and Technologies for Geosciences*, edited by V. Demyanov and J. Becedas, IntechOpen, Rijeka, 2020, Chap. 8. https://doi.org/10.5772/intechopen.92625, URL https://doi.org/10.5772/intechopen.92625.
- [2] Chalia, S., Bharti, M. K., Thakur, P., Thakur, A., and Sridhara, S., "An overview of ceramic materials and their composites in porous media burner applications," *Ceramics International*, Vol. 47, No. 8, 2021, pp. 10426–10441.
- [3] Sommers, A., Wang, Q., Han, X., T'Joen, C., Park, Y., and Jacobi, A., "Ceramics and ceramic matrix composites for heat exchangers in advanced thermal systems—A review," *Applied Thermal Engineering*, Vol. 30, No. 11-12, 2010, pp. 1277–1291.
- [4] Zhang, B., Wang, H., Jin, X., Fan, X., Huang, H., and Yao, J., "Novel C/SiC porous ceramic with controllable properties served as transpiration cooling material," *Ceramics International*, 2022.
- [5] Armstrong, I. W., "Development and Testing of Additively Manufactured Aerospike Nozzles for Small Satellite Propulsion," Master's thesis, Utah State University, 2019. URL https://www.proquest.com/dissertations-theses/development-testing-additively-manufactured/docview/2179114932/se-2?accountid=10267.
- [6] Klocke, F., "Modern approaches for the production of ceramic components," *Journal of the European Ceramic Society*, Vol. 17, No. 2-3, 1997, pp. 457–465.
- [7] Lakhdar, Y., Tuck, C., Binner, J., Terry, A., and Goodridge, R., "Additive manufacturing of advanced ceramic materials," *Progress in Materials Science*, Vol. 116, 2021, p. 100736.
- [8] Hu, K., Wei, Y., Lu, Z., Wan, L., and Li, P., "Design of a Shaping System for Stereolithography with High Solid Loading Ceramic Suspensions," 3D Printing and Additive Manufacturing, Vol. 5, 2018, pp. 311–318. https://doi.org/10.1089/3DP.2017. 0065/ASSET/IMAGES/LARGE/FIGURE9.JPEG, URL https://www.liebertpub.com/doi/full/10.1089/3dp.2017.0065.
- [9] Altun, A. A., Prochaska, T., Konegger, T., and Schwentenwein, M., "Dense, strong, and precise silicon nitride-based ceramic parts by lithography-based ceramic manufacturing," *Applied Sciences (Switzerland)*, Vol. 10, 2020. https://doi.org/10.3390/app10030996.
- [10] Miles, P., A., Dodge, M., J., Ballard, S., S., Browder, J., S., Feldman, A., and Weber, M., J., "Optical Materials Part 2: Properties," *Handbook of Optical Materials*, Vol. IV, CRC Press, New York, 2003, pp. 17–107.
- [11] Maheswara, M., Oh, S.-H., Ju, J.-J., Park, S. K., Park, S., and Do, J. Y., "High refractive index of transparent acrylate polymers functionalized with alkyl sulfur groups," *Polym J*, Vol. 42, No. 3, 2010, pp. 249–255. https://doi.org/10.1038/pj.2009.328, URL https://www.nature.com/articles/pj2009328, number: 3 Publisher: Nature Publishing Group.
- [12] Xue, L. A., and Chen, I.-W., "Low-Temperature Sintering of Alumina with Liquid-Forming Additives," *Journal of the American Ceramic Society*, Vol. 74, No. 8, 1991, pp. 2011–2013. https://doi.org/10.1111/j. 1151-2916.1991.tb07825.x, URL https://onlinelibrary.wiley.com/doi/abs/10.1111/j.1151-2916.1991.tb07825.x, \_eprint: https://onlinelibrary.wiley.com/doi/pdf/10.1111/j.1151-2916.1991.tb07825.x.
- [13] Halloran, J. W., "Ceramic Stereolithography: Additive Manufacturing for Ceramics by Photopolymerization," 2016. https://doi.org/10.1146/annurev-matsci-070115-031841, URL www.annualreviews.org.
- [14] Sbaizero, O., and Pezzotti, G., "Influence of molybdenum particles on thermal shock resistance of alumina matrix ceramics," *Materials Science and Engineering: A*, Vol. 343, No. 1, 2003, pp. 273–281. https://doi.org/https://doi.org/10.1016/S0921-5093(02)00370-2, URL https://www.sciencedirect.com/science/article/pii/S0921509302003702.
- [15] "Standard Test Method for Determination of Thermal Shock Resistance for Advanced Ceramics by Water Quenching," Standard ASTM C1525-18, ASTM International, July 2018.
- [16] Hampshire, S., "Silicon nitride ceramics-review of structure, processing and properties," *Journal of Achievements in Materials and Manufacturing Engineering*, 2007.
- [17] Li, X., Zhang, J., Duan, Y., Liu, N., Jiang, J., Ma, R., Xi, H., and Li, X., "Rheology and curability characterization of photosensitive slurries for 3D printing of Si3N4 ceramics," *Applied Sciences (Switzerland)*, Vol. 10, 2020. https://doi.org/10.3390/APP10186438.
- [18] Malitson, I. H., "Interspecimen Comparison of the Refractive Index of Fused Silica\*,†," *JOSA*, Vol. 55, No. 10, 1965, pp. 1205–1209. https://doi.org/10.1364/JOSA.55.001205, URL https://opg.optica.org/josa/abstract.cfm?uri=josa-55-10-1205, publisher: Optica Publishing Group.

- [19] Malitson, I. H., Murphy, F. V., and Rodney, W. S., "Refractive Index of Synthetic Sapphire," *JOSA*, Vol. 48, No. 1, 1958, pp. 72–73. https://doi.org/10.1364/JOSA.48.000072, URL https://opg.optica.org/josa/abstract.cfm?uri=josa-48-1-72, publisher: Optica Publishing Group.
- [20] Luke, K., Okawachi, Y., Lamont, M. R. E., Gaeta, A. L., and Lipson, M., "Broadband mid-infrared frequency comb generation in a Si<sub>3</sub>N<sub>4</sub> microresonator," *Optics Letters*, Vol. 40, No. 21, 2015, pp. 4823–4826. https://doi.org/10.1364/OL.40.004823, URL https://opg.optica.org/ol/abstract.cfm?uri=ol-40-21-4823, publisher: Optica Publishing Group.
- [21] Pastrňák, J., and Roskovcová, L., "Refraction Index Measurements on AlN Single Crystals," physica status solidi (b), Vol. 14, No. 1, 1966, pp. K5–K8. https://doi.org/10.1002/pssb.19660140127, URL https://onlinelibrary.wiley.com/doi/abs/10.1002/pssb.19660140127, \_eprint: https://onlinelibrary.wiley.com/doi/pdf/10.1002/pssb.19660140127.
- [22] Larruquert, J. I., Pérez-Marín, A. P., García-Cortés, S., Marcos, L. R.-d., Aznárez, J. A., and Méndez, J. A., "Self-consistent optical constants of SiC thin films," *JOSA A*, Vol. 28, No. 11, 2011, pp. 2340–2345. https://doi.org/10.1364/JOSAA.28.002340, URL https://opg.optica.org/josaa/abstract.cfm?uri=josaa-28-11-2340, publisher: Optica Publishing Group.
- [23] Montanari, C., "Additive Manufacturing of Silicon Nitride," Master's thesis, Luleå University of Technology, Luleå, Sweden, 2017.
- [24] Huang, R.-J., Jiang, Q.-G., Wu, H.-D., Li, Y.-H., Liu, W.-Y., Lu, X.-X., and Wu, S.-H., "Fabrication of complex shaped ceramic parts with surface-oxidized Si3N4 powder via digital light processing based stereolithography method," *Ceramics International*, Vol. 45, No. 4, 2019, pp. 5158–5162.
- [25] Yang, P., Sun, Z., Huang, S., Ou, J., Jiang, Q., Li, D., and Wu, S., "Digital light processing 3D printing of surface-oxidized Si3N4 coated by silane coupling agent," *Journal of Asian Ceramic Societies*, Vol. 10, No. 1, 2022, pp. 69–82. https://doi.org/10.1080/21870764.2021.2009096, URL https://doi.org/10.1080/21870764.2021.2009096, publisher: Taylor & Francis \_eprint: https://doi.org/10.1080/21870764.2021.2009096.
- [26] Lin, L., Wu, H., Xu, Y., Lin, K., Zou, W., and Wu, S., "Fabrication of dense aluminum nitride ceramics via digital light processing-based stereolithography," *Materials Chemistry and Physics*, Vol. 249, 2020, p. 122969. https://doi.org/10.1016/J. MATCHEMPHYS.2020.122969.
- [27] Ożóg, P., Rutkowski, P., Kata, D., and Graule, T., "Ultraviolet Lithography-Based Ceramic Manufacturing (UV-LCM) of the Aluminum Nitride (AlN)-Based Photocurable Dispersions," *Materials* 2020, Vol. 13, Page 4219, Vol. 13, 2020, p. 4219. https://doi.org/10.3390/MA13194219, URL https://www.mdpi.com/1996-1944/13/19/4219/htmhttps://www.mdpi.com/1996-1944/13/19/4219.
- [28] "Standard Test Method for Flexural Strength of Advanced Ceramics at Ambient Temperature," Standard ASTM C1161-18, ASTM International, October 2018.
- [29] Sarin, V. K., "On the -to- phase transformation in silicon nitride," Materials Science and Engineering: A, Vol. 105-106, 1988, pp. 151–159. https://doi.org/10.1016/0025-5416(88)90491-0, URL https://www.sciencedirect.com/science/article/pii/0025541688904910.
- [30] Richerson, D., Richerson, D. W., and Lee, W. E., Modern Ceramic Engineering: Properties, Processing, and Use in Design, Third Edition, CRC Press, 2005.